applied optics

Surface-enhanced coherent anti-Stokes Raman imaging of lipids

Alexander Fast,[1] John P. Kenison,[2] Christopher D. Syme,[3] and Eric O. Potma[1,*]

[1]Department of Chemistry, University of California, Irvine, California 92697, USA
[2]Department of Physics and Astronomy, University of California, Irvine, California 92697, USA
[3]Department of Chemistry, University of Glasgow, Glasgow G12 8QQ, UK
*Corresponding author: epotma@uci.edu

Received 13 May 2016; revised 27 June 2016; accepted 30 June 2016; posted 1 July 2016 (Doc. ID 265073); published 27 July 2016

This work describes in detail a wide-field surface-enhanced coherent anti-Stokes Raman scattering (CARS) microscope, which enables enhanced detection of sample structures in close proximity (~100 nm) of the substrate interface. Unlike conventional CARS microscopy, where the sample is illuminated with freely propagating light, the current implementation uses evanescent fields to drive Raman coherences across the entire object plane. By coupling the pump and Stokes excitation beams to the surface plasmon–polariton mode at the interface of a 30 nm thick gold film, we obtained strong CARS signals from cholesteryl oleate droplets adhered to the surface. The surface-enhanced CARS imaging system visualizes lipid structures with vibrational selectivity using illumination doses per unit area that are more than four orders of magnitude lower than in point-scanning CARS microscopy.

OCIS codes: (180.4315) Nonlinear microscopy; (190.4380) Nonlinear optics, four-wave mixing; (190.4710) Optical nonlinearities in organic materials; (190.5650) Raman effect.

http://dx.doi.org/10.1364/AO.55.005994

1. INTRODUCTION

Coherent Raman scattering (CRS) microscopy has long been recognized as a useful label-free tool for visualizing lipids in biological samples [1–3]. The organization of lipophilic compounds into densely packed structures gives rise to a high local concentration of methylene groups in tissues and cells, which produces strong and detectable CRS signals when driven at the C-H stretching vibrational energies. Not surprisingly, the micrometer-sized intracellular organelles comprised of neutral lipids, also known as lipid droplets, have been a prime target for CRS imaging [4–7]. Because the volume of lipid droplets is on the order of the focal volume in the CRS microscope, the number of driven methylene groups is high, often exceeding 10^{10} CH_2 units. The strong coherent Raman signals thus generated have greatly facilitated the study of these organelles.

Cell membranes, which contain phospholipids and other constituents organized into bilayers, are also a natural object of study for coherent Raman imaging techniques. The number of methylene groups that a single bilayer adds to the focal volume, however, is in the 10^6 range [8], which is orders of magnitude lower than the numbers found in lipid droplets. Consequently, it can be challenging to visualize membranes with CRS. Several studies of phospholipid bilayers *in vitro* have successfully used CRS for imaging and spectroscopy, emphasizing that single bilayer sensitivity can be reached in controlled environments [8–11]. In cells, it is more difficult to discern the membrane-specific CRS signal because it is often overwhelmed by accompanying background contributions, including the resonant coherent Raman signals from other organic compounds in the cell. Certain intracellular membrane structures can be discerned in the cell, most notably the nuclear envelope [12], but visualizing the plasma membrane, for instance, has remained a challenge.

One of the reasons why a planar membrane does not yield a clear and specific CRS signal in a heterogeneous environment is that the focal volume encompasses many other constituents that contribute to the signal. A planar lipid bilayer is about 7 nm thick, whereas the probing volume extends over hundreds of nanometers. Decreasing the probing volume is a potential strategy to improve the specificity of the CRS microscope for imaging cell membranes *en face*. Reducing the probing volume can be achieved by confining the excitation fields to the vicinity of the glass/sample interface, such as is the case in total internal reflection fluorescence (TIRF) microscopy [13,14]. In TIRF microscopy, excitation is accomplished with evanescent fields, which are confined to the glass/sample interface. Unlike signals induced by freely propagating light, the use of evanescent excitation fields rejects signal contributions from the bulk

of the cell. Because of these favorable imaging properties, TIRF has become the method of choice to study planar cell membranes with fluorescent probes.

Using a wide-field evanescent illumination scheme, as is used in TIRF, is not straightforward in CRS microscopy. First, at least two propagating laser beams must be coupled to the evanescent mode at the glass/sample interface, necessitating rather complex illumination schemes. Second, the density of the excitation field must be sufficient to induce a third-order response in the sample. The pulse power required to reach these limits may not be readily available from the high repetition rate light sources that are typically used in CRS microscopy. The latter limitation can be overcome by using the enhancement effects of surface plasmon modes. As early as 1979, it was shown that the confined surface fields of surface plasmon–polaritons (SPP) at a thin silver layer can be used to generate a coherent anti-Stokes Raman scattering (CARS) signal from a liquid in contact with the metal film [15]. This principle was recently extended for imaging, where the SPP fields at the metal/sample interface were able to generate four-wave mixing (FWM) signals from nanostructures in a wide-field imaging geometry [16].

So far, the concept of surface-enhancement at planar metal interfaces has not yet been used to visualize structures with vibrationally sensitive CRS. This work describes an objective-based, wide-field CARS microscope with evanescent illumination. The CARS signal is surface-enhanced over the entire field of view by coupling the pump and Stokes excitation beams to the SPP modes supported by a 30 nm gold film deposited on a glass coverslip. We demonstrate that lipid structures on the gold film are readily visualized with CARS, and that the observed signal is vibrationally sensitive. Since the signal originates solely from the evanescent excitation volume close to the interface, the SPP-based CARS microscope uniquely adds surface sensitivity to the existing imaging capabilities of CRS microscopy.

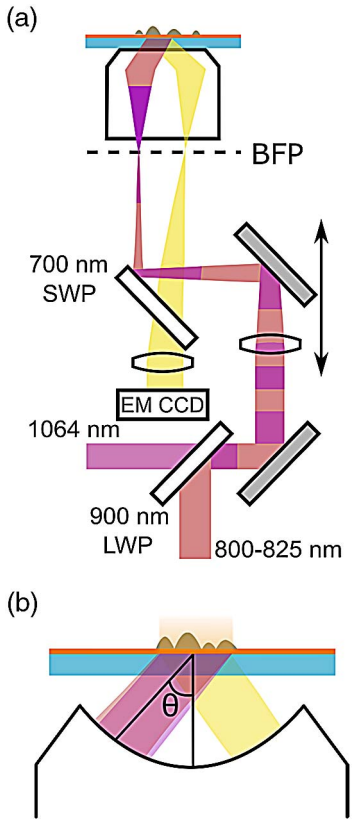

Fig. 1. Schematic of the wide-field, surface-enhanced CARS microscope. (a) Quasi-collinear pump and Stokes beams are focused on the back focal plane (BFP) of the microscope objective, resulting in sample illumination with collimated beams. (b) Objective-based excitation of SPP modes at the Kretschmann angle. Angle of incidence θ is controlled by adjusting the lateral position of the beams at the BFP of the microscope objective.

2. MATERIALS AND METHODS

A. Microscope Setup

The laser source used in our experiments here consists of a 76 MHz Nd-Vanadate amplified oscillator (PicoTrain, High-Q), which produces 7 ps pulses at a center wavelength of 1064 nm. A portion of the laser output was used as the Stokes beam in the CARS process. Another portion of the output was frequency doubled and used to synchronously pump an optical parametric oscillator (OPO, Levante Emerald, APE-Berlin). The latter delivers tunable radiation in the 750–950 nm range. For our CARS experiments, we used the OPO from 800 to 825 nm, delivering the pump radiation for the CARS process. The Raman shift in this study was tuned to the 2750–3000 cm^{-1} spectral range, corresponding to the energy of the C-H vibrational stretches.

The pump and Stokes beams were separately conditioned with spatial filters and expanded to a ~7 mm beam diameter. Both beams exhibit Gaussian transverse profiles that are linearly polarized. The beams were quasi-collinearly overlapped in space and time on a dichroic mirror (Chroma LWP 900 nm). The alignment allowed for a small angular difference between the beams, as dictated by the different plasmon coupling angles of the pump and Stokes beams. The combined beams were focused with a 200 mm achromatic lens (Edmund Optics) on the back focal plane (BFP) of a 60 × 1.49 NA oil immersion objective, (APON60XOTIRF, Olympus) providing wide-field illumination [Fig. 1(a)]. A movable mirror made it possible to translate the lateral position of the focused spot on the BFP, resulting in an angular adjustment of the collimated beams incident on the sample [Fig. 1(b)]. The CARS radiation was detected in the epi-direction and separated from the incident light by a dichroic mirror (Semrock SWP 700 nm). Radiation from the sample plane was projected onto an imaging EM CCD (Andor iXon) camera using two bandpass filters (Chroma ET660/40) to isolate the CARS signal.

In this configuration, we could estimate the diameter d of the illuminated field of view (FOV) from

$$d_{\mathrm{FOV}} = d_{\mathrm{beam}} \frac{\mathrm{FL}_{\mathrm{objective\ lens}}}{\mathrm{FL}_{\mathrm{focusing\ lens}}}, \quad (1)$$

where FL denotes focal length. In the experiments described here, the FOV was set as 105 μm × 105 μm. Average power at the sample was 60 mW for each beam for the entire

FOV, corresponding to 11 μW per μm^2. Images were taken with a 1 s integration time in the electron multiplication acquisition mode.

B. Sample Preparation

Sample substrates consisted of borosilicate glass coverslips (BK-7, VWR) coated with gold. Gold thin films were evaporated to a thickness of 30 nm on the coverslips, which were pretreated with a 2 nm Cr adhesion layer. For patterned Au films, lithographic masks were used to deposit S1808 photoresist (Shipley) onto the surface, followed by chemical etching. For a subset of experiments in this work, patterns consisting of 20 μm wide Au stripes, with a spacing of 20 μm between the stripes, were fabricated.

The lipid samples used in the experiments were droplets and crystals of cholesteryl oleate (Sigma Aldrich). The droplets were formed by preparing an emulsion of cholesteryl oleate with phosphatidylcholine in phosphate-buffered saline (PBS). Using ~50 μL of a stock solution, the emulsion was subsequently spin coated on the Au-covered microscope coverslips, resulting in air-dried droplets and micrometer-sized polymorphous crystals of cholesteryl oleate on the surface.

3. EXPERIMENTAL RESULTS

A. Wide-Field Excitation of SPP Modes

The working principle of the wide-field, surface-enhanced CARS microscope is based on the excitation of the sample by the evanescent fields of plasmon modes at the gold/air interface. To generate the surface-bound excitation field, the freely propagating pump and Stokes beams have to be coupled to the surface plasmon mode. We have chosen an objective-based Kretschmann configuration, in which both the pump and Stokes beams are incident on the gold/air interface at their respective SPP coupling angles of $\theta_{\text{pump}} = 42.3°$ and $\theta_{\text{Stokes}} = 42.7°$ for a Raman shift of 2841 cm^{-1}.

We facilitated the alignment of the beams by monitoring the back reflection of the excitation beams onto the CCD camera. Figure 2 shows the back reflection of the pump beam at 817 nm incident on a striped gold film. In Fig. 2(a), the coupling angle is below the Kretschmann angle, resulting in a strong reflection at the gold stripe (bright) and a weak reflection from the bare glass (dark). When the incident angle was tuned to $\theta_{\text{pump}} = 42.3°$, phase matching with the SPP mode occurred and energy was transferred from the freely propagating mode to the surface-bound mode. The latter can be inferred from Fig. 2(b), which shows greatly reduced reflection at the gold stripe, whereas the signal from the exposed glass is elevated due to total internal reflection. As in previous surface plasmon resonance microscopy studies [17], we achieved efficient SPP coupling over the entire FOV.

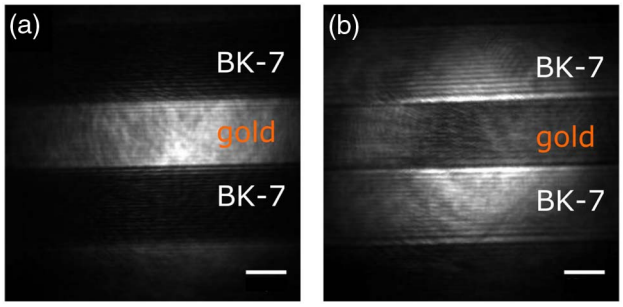

Fig. 2. Coupling of light to SPP at the gold film–air interface. Reflection image of the pump beam at 41°, (a) before light couples and (b) at 42.3° when energy transfer to the SPP mode occurs. Scale bars are 20 μm.

B. Surface-enhanced CARS of Lipid

We next considered the CARS signal radiated by cholesteryl oleate structures on the striped gold substrate. In this experiment, both the pump and Stokes beams were coupled at their respective Kretschmann angles. Figure 3(a) shows the resulting CARS signal seen on the CCD camera, superimposed on a light transmission image (gray tones). The CARS image shows three bright spots, corresponding to condensed cholesteryl oleate structures, obtained at the on-resonance Raman shift of 2841 cm^{-1}. The transmission image reveals that the three spots were located on top of the gold stripe. Note that no CARS signal was seen from the areas that correspond to the bare glass surface, even though lipid material can be seen in these regions in the transmission image. The latter observation indicates that the CARS signal was only visible when surface-enhanced by the gold layer, similar to what was previously observed for surface-enhanced FWM imaging [16].

In addition to CARS radiation, we observed a two-photon excited luminescent (TPEL) background from the regions covered by the Au film. We attributed this pump-induced signal from SPP-enhanced interband transitions in the gold, followed by electron-hole radiative recombination [18]. In the images shown, the TPEL background was subtracted by separately recording an image with the pump only and normalizing as

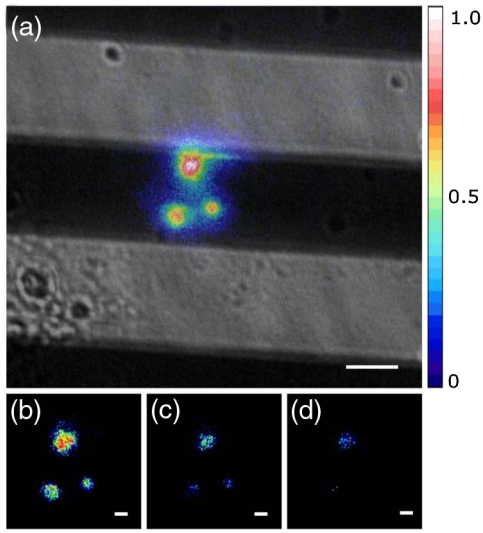

Fig. 3. CARS from cholesteryl oleate structures are observed only when in close proximity of the Au film. (a) CARS image (rainbow colors) at 2841 cm^{-1} superimposed onto a transmission image (gray tones). Brighter areas in the transmission image correspond to bare glass, darker regions to the 30 nm gold film. (b) Zoomed in area at 2841 cm^{-1}, (c) 2782 cm^{-1}, and (d) 2768 cm^{-1}. Scale bars are (a) 20 μm and (b–d) 5 μm.

$$I_{\mathrm{CARS}} = \frac{I_{\mathrm{Total}} - I_{\mathrm{TPEL}}}{I_{\mathrm{TPEL}}}. \quad (2)$$

This operation accounted for variations in the pump-coupling efficiency by using the broadband TPEL signal as a reference.

The lipid structures in the CARS image of Fig. 3(a) appear surrounded by a weak CARS emission. In addition, part of the weaker CARS signal is emanating from the edge of the gold film. We attribute these weaker contributions to the coupling of anti-Stokes radiation, generated at the lipid, back into the film [19]. Part of the surface-bound anti-Stokes field can couple out as leakage radiation directly from the film, as well as at the edges.

The detected CARS radiation showed the expected dependence on the vibrational energy. Figures 3(b)–3(d) depict the zoomed-in area of the three bright spots for various Raman shifts. The signal measured at 2841 cm^{-1} (b), resonant with the CH_2 symmetric stretching mode, was stronger than the signal measured at the off-resonant energies of 2782 cm^{-1} (c) and 2768 cm^{-1} (d).

C. Signal Contributions in Surface-enhanced CARS Imaging

The striped gold film clearly revealed that surface-enhanced CARS contributions dominate the detected signal. Nonetheless, we saw some artifacts at the film's edges. In Fig. 4, we observed a cluster of cholesteryl oleate structures on a continuous gold film, which eliminated the edge artifacts. The on-resonance signal shown in Fig. 4(a) is significantly stronger than the off-resonance signal shown in 4B. Nonetheless, the ratio of resonant (2841 cm^{-1}) to nonresonant (2768 cm^{-1}) CARS is about 2:1, which is less than commonly observed for the CH_2 symmetric stretching mode when imaged with freely propagating light. This observation underlines the likelihood of FWM contributions from the gold layer, and that the coupling of these nonresonant field contributions to the far-field is enhanced in the vicinity of the lipid structures, thus producing a nonresonant background signal. Although the images in Fig. 4 clearly show that resonant CARS signals can be detected, attempts to suppress the nonresonant contributions from the gold would be desirable to improve the imaging contrast.

As in Fig. 3, a weak CARS signal around the structures is also discernible in Fig. 4. However, this background signal is weaker when the Raman shift is tuned to off-resonance

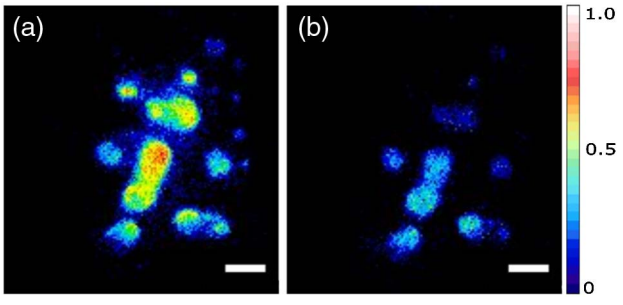

Fig. 4. CARS images of cholesteryl oleate structures highlighting features resonant at (a) 2841 cm^{-1} and (b) 2768 cm^{-1}. Scale bar is 20 μm.

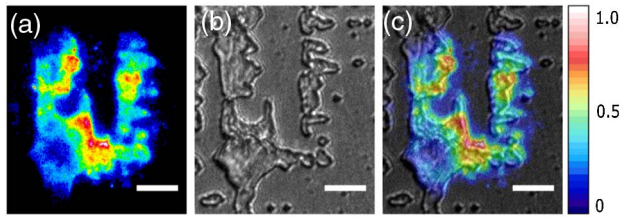

Fig. 5. CARS image (rainbow) of a thick aggregate of cholesteryl oleate taken at (a) 2841 cm^{-1}, (b) transmission image (gray), and (c) and overlay of CARS and corresponding transmission images. Scale bar is 20 μm.

vibrational energies, and thus cannot be attributed to an independent FWM signal from the gold layer. This indicates that the weak background scales with the strength of the signal (both resonant and nonresonant) generated at the location of the lipid structures, which is back-coupled into the film.

Figure 5 provides another look at the weak CARS signal that appears away from the lipid. The surface-enhanced CARS signal from thick cholesteryl oleate deposits is shown in Fig. 5(a), and is compared with the corresponding transmission image. The overlay in Fig. 5(c) emphasizes that a weak CARS signal can be detected from regions where no (thick) lipid structures are present. Note that this imaging property is markedly different from the imaging properties when using freely propagating light, and somewhat complicates the determination of the lateral resolution in surface-enhanced CARS imaging.

4. DISCUSSION

In this work, we modified a wide-field FWM microscope to perform surface-sensitive CARS measurements. The current microscope operates in the wide-field illumination and imaging mode. This mode shares similarities with previous wide-field CARS [20–23] and FWM microscopes [24]. Nonetheless, we believe the current design differs in an important way from previous wide-field designs in that it incorporates the concept of surface enhancement. Instead of using propagating radiation to drive Raman coherences in the sample, the surface-enhanced CARS microscope employs the evanescent fields associated with the SPP modes in a thin gold film for exciting the Raman modes. This principle enables the following novel aspects to be implemented in CARS imaging: (1) the CARS signal is intrinsically confined to the region close to the gold/sample interface, thus giving the microscope "surface-sensitive" properties, and (2) the CARS signal is boosted due to the field enhancement effect of the surface plasmon mode.

In the current implementation, the CARS signals originate from the region close to the gold/sample interface. In the direction normal to the planar interface, the CARS efficiency decreases exponentially away from the surface characterized by a 1/e distance of ~100 nm [16]. For some of the thicker structures imaged in this work, this implies that the surface-enhanced CARS signal does not originate from the entire structure, as only the first ~100 nm of the sample contributes to the detected signal. We noted that the magnitude of surface-enhanced CARS signals from the lipid structures was virtually

uniform, regardless of the size of the (sub-)μm-sized structure, which is further proof that only the part of the structure close to the substrate interface is probed in this excitation geometry. The bulk of the structure was rejected, an imaging property desired for future experiments on cells.

The surface-enhancement effect is essential for observing CARS signals from lipids close to the interface. In the absence of the 30 nm gold layer, no CARS signals are observed under the current excitation conditions. The importance of surface-enhancement is underscored by a quick comparison between CARS imaging with freely propagating beams and with evanescent fields at a planar interface. In regular CARS microscopy, an average power of 10 mW per beam is common to visualize lipid structures, assuming ps pulses and a 76 MHz repetition rate. Using a high NA microscope objective, and assuming a spot size with a 0.3 μm diameter, the pulse energy for each beam is ~2 nJ/μm^2. Similar pulse energies per unit area are needed to generate detectable CARS signals in wide-field excitation geometries without surface-enhancement [22]. By comparison, in our wide-field CARS configuration with SPP excitation, an average beam power of 60 mW translated into a pulse energy of 70 fJ/μm^2. This implies that the illumination density per beam is more than four orders of magnitude lower in surface-enhanced CARS imaging, yet the strength of the CARS signal is comparable to that seen in conventional CARS microscopy. The implications for surface-enhanced CARS imaging are clear: detectable CARS signals can be observed at much lower average power per unit area, making it possible to perform wide-field CARS imaging with standard high-repetition rate lasers and moderate pulse energies. In addition, lower pulse energies also help to reduce tentative linear and nonlinear heating of the sample, as may occur when illuminating with high energy pulses.

Recent literature includes several reports of surface-enhanced CARS experiments. Examples include enhanced CARS signals at atomic tips [25,26], colloidal particles [27–29], and specially prepared metallic nanostructures [30–32]. These studies make it clear that, similar to surface-enhanced Raman scattering (SERS), the surface enhancement effect in coherent Raman can be leveraged to boost molecular signals, even at the single molecule limit [29,33,34]. Unlike previous surface-enhanced CARS studies, where the CARS signal emerges from selected hotspots only, here we used the surface-enhancement effect to amplify the signal generation efficiency of an entire CARS image. Instead of using localized surface plasmons, we used SPP modes at the planar interface between a gold film and the sample.

Although the use of a gold film raised the CARS signal by orders of magnitude, it also introduced imaging artifacts that are absent in CARS imaging with freely propagating light. First, the gold layer is a highly polarizable material, which exhibits its own third-order optical response. It is, therefore, perhaps remarkable that the surface-enhanced CARS images are not overwhelmed by a strong coherent FWM signal from the gold substrate [35–38]. We found that in the configuration we examined, the nonlinear coherent polarization at the $2\omega_p - \omega_S$ frequency in the gold layer did not efficiently couple to the far-field detector. Instead, we observed that the strongest background signal stems from the incoherent TPEL of the gold, which is enhanced by the strong evanescent excitation fields. In practice, the TPEL can be removed relatively easily by subtracting the pump-only signal from the image induced by both pump and Stokes beams. We also observed a weak CARS signal that surrounded the response of the lipid structures, a contribution that appeared to originate from resonant and nonresonant signal contributions generated at the location of the lipid structures that are back-coupled into the gold film.

Finally, we noticed that the off-resonant CARS signal from the lipid structures is higher than commonly observed in laser-scanning CARS microscopy. This effect may be attributed to the enhanced coupling of the gold's FWM response to the far field at the location of the lipid structures. The presence of the structures perturbs the local fields and may thus alter the radiative properties of the film at these locations. We expect the latter effect to be negligible when imaging is performed on membranes in an aqueous environment, in which case the spatial variations in the sample's linear and nonlinear refractive index are significantly smaller than for the air-exposed sample studied here.

In this work, we used CARS as the contrast mechanism to visualize lipid structures. An alternative method is stimulated Raman scattering (SRS) microscopy, which, using freely propagating light, has been shown to produce images devoid of nonresonant background contributions [2,39,40]. Implementing SRS for the purpose of surface-sensitive imaging is, however, more complicated in the wide-field geometry pursued in this study. Because SRS relies on detecting a small gain or loss of the incident beams, nontrivial demodulation techniques are required when using a CCD camera as the photodetector. In addition, it is not clear if SRS offers clear advantages over CARS when used in combination with surface enhancement. Recent studies have revealed that surface-enhanced SRS is not free from the nonresonant response from the metal, as evidenced by dispersive line shapes observed in broadband SRS experiments [41,42]. For these reasons, we chose CARS as the contrast mechanism for selectively visualizing lipid structures close to the interface.

The implementation discussed here uses a coupling geometry for samples that are air exposed. Our main motivation was to demonstrate that vibrationally sensitive CARS images can be obtained from lipid structures near the interface. Nonetheless, the more challenging goal of visualizing cell membranes in aqueous environments requires adjusted angles and beam geometries for coupling the propagating pump and Stokes beams to the SPP modes. We expect that once the system is optimized for imaging of aqueous samples, surface-enhanced CARS microscopy may offer the sensitivity needed to visualize planar cell membranes.

5. CONCLUSION

We have demonstrated that surface-enhanced CARS microscopy with wide-field illumination and detection can visualize lipid structures at interfaces. The signal strength and image acquisition time of surface-enhanced CARS microscopy is comparable to that of conventional point-scanning CARS microscopy, yet the power density per unit area of the excitation beams

is reduced by more than four orders of magnitude. With its improved signal rejection from the bulk, SPP-mediated CARS microscopy holds promise as a label-free imaging tool for the plasma membrane of live cells.

Funding. National Science Foundation (NSF) (1454885); Engineering and Physical Sciences Research Council (EPSRC) (EP/J004790/1); SFC PECRE (WestCHEM).

Acknowledgment. We thank Shaopeng Qiao for help with fabricating the gold-coated coverslips.

REFERENCES

1. T. T. Le, S. Yue, and J.-X. Cheng, "Shedding new light on lipid biology with coherent anti-Stokes Raman scattering microscopy," J. Lipid Res. **51**, 3091–3102 (2010).
2. J.-X. Cheng and X. S. Xie, *Coherent Raman Scattering Microscopy* (CRC, 2013).
3. C. Zhang, D. Zhang, and J.-X. Cheng, "Coherent Raman scattering microscopy in biology and medicine," Ann. Rev. Biomed. Eng. **17**, 415–445 (2015).
4. X. Nan, J.-X. Cheng, and X. S. Xie, "Vibrational imaging of lipid droplets in live fibroblast cells with coherent anti-Stokes Raman scattering microscopy," J. Lipid Res. **44**, 2202–2208 (2003).
5. H.-W. Wang, Y. Fu, T. B. Huff, T. T. Le, H. Wang, and J.-X. Cheng, "Chasing lipids in health and diseases by coherent anti-Stokes Raman scattering microscopy," Vib. Spectrosc. **50**, 160–167 (2009).
6. A. Enejder, C. Brackmann, and F. Svedberg, "Coherent anti-Stokes Raman Scattering microscopy of cellular lipid storage," IEEE J. Sel. Top. Quantum Electron. **16**, 506–515 (2010).
7. N. Billecke, G. Rago, M. Bosma, G. Eijkel, A. Gemmink, P. Leproux, G. Huss, P. Schrauwen, M. K. C. Hesselink, M. Bonn, and S. H. Parekh, "Chemical imaging of lipid droplets in muscle tissues using hyperspectral coherent Raman microscopy," Histochem. Cell Biol. **141**, 263–273 (2014).
8. E. Potma and X. S. Xie, "Detection of single lipid bilayers with coherent anti-Stokes Raman scattering (CARS) microscopy," J. Raman Spectrosc. **34**, 642–650 (2003).
9. E. Potma and X. S. Xie, "Direct visualization of lipid phase segregation in single lipid bilayers with coherent anti-Stokes Raman scattering microscopy," Chem. PhysChem **6**, 77–79 (2005).
10. G. W. H. Wurpel, J. M. Schins, and M. Müller, "Direct measurement of chain order in single phospholipid mono- and bilayers with multiplex CARS," J. Phys. Chem. B **108**, 3400–3403 (2004).
11. L. Li, H. Wang, and J.-X. Cheng, "Quantitative coherent anti-Stokes Raman scattering imaging of lipid distribution in coexisting domains," Biophys. J. **89**, 3480–3490 (2005).
12. J.-X. Cheng, Y. K. Chia, G. Zheng, and X. S. Xie, "Laser-scanning coherent anti-Stokes Raman scattering microscopy and applications to cell biology," Biophys. J. **83**, 502–509 (2002).
13. D. Axelrod, T. P. Burghardt, and N. L. Thompson, "Total internal reflection fluorescence," Ann. Rev. Biophys. Bioeng. **13**, 247–268 (1984).
14. D. Axelrod, "Total internal reflection fluorescence microscopy in cell biology," Traffic **2**, 764–774 (2001).
15. C. K. Chen, A. R. B. de Castro, Y. R. Shen, and F. DeMartini, "Surface coherent anti-Stokes Raman spectroscopy," Phys. Rev. Lett. **43**, 946–949 (1979).
16. Y. Wang, X. Liu, A. R. Halpern, K. Cho, R. M. Corn, and E. O. Potma, "Wide-field, surface-sensitive four-wave mixing microscopy of nanostructures," Appl. Opt. **51**, 3305–3312 (2012).
17. A. R. Halpern, J. B. Wood, Y. Wang, and R. M. Corn, "Single-nanoparticle near-infrared surface plasmon resonance microscopy for real-time measurements of DNA hybridization adsorption," ACS Nano **8**, 1022–1030 (2014).
18. G. T. Boyd, Z. H. Lu, and Y. R. Shen, "Photoinduced luminescence from the noble metals and its enhancement on roughened surfaces," Phys. Rev. B **33**, 7923–7936 (1986).
19. X. Liu, Y. Wang, and E. O. Potma, "Surface-mediated four-wave mixing of nanostructures with counterpropagating surface plasmon polaritons," Opt. Lett. **36**, 2348–2350 (2011).
20. C. Heinrich, S. Bernet, and M. Ritsch-Marte, "Wide-field coherent anti-Stokes Raman scattering microscopy," Appl. Phys. Lett. **84**, 816–818 (2004).
21. I. Toytman, K. Cohn, T. Smith, D. Simanovskii, and D. Palanker, "Wide-field coherent anti-Stokes Raman scattering microscopy with non-phase-matching illumination," Opt. Lett. **32**, 1941–1943 (2007).
22. I. Toytman, D. Simanovskii, and D. Palanker, "On illumination schemes for wide-field CARS microscopy," Opt. Express **17**, 7339–7347 (2009).
23. P. Berto, A. Jesacher, C. Roider, S. Monneret, H. Rigneault, and M. Ritsch-Marte, "Wide-field vibrational phase imaging in an extremely folded box-CARS geometry," Opt. Lett. **38**, 709–711 (2013).
24. J. Koivistoinen, J. Aumanen, V.-M. Hiltunen, P. Myllyperkiö, A. Johansson, and M. Pettersson, "Real-time monitoring of graphene patterning with wide-field four-wave mixing microscopy," Appl. Phys. Lett. **108**, 153112 (2016).
25. T. Ichimura, N. Hayazawa, M. Hashimoto, Y. Inouye, and S. Kawata, "Tip-enhanced coherent anti-Stokes Raman scattering for vibrational nanoimaging," Phys. Rev. Lett. **92**, 220801 (2004).
26. M. Namboodiri, T. Khan, K. Karki, M. M. Kazemi, S. Gom, G. Flachenecker, V. Namboodiri, and A. Materny, "Nonlinear spectroscopy in the near-field: time resolved spectroscopy and subwavelength resolution non-invasive imaging," Nanophotonics **3**, 61–73 (2014).
27. E. J. Liang, A. Weippert, J. M. Funk, A. Materny, and W. Kiefer, "Experimental observation of surface-enhanced coherent anti-Stokes Raman scattering," Chem. Phys. Lett. **227**, 115–120 (1994).
28. T. Ichimura, N. Hayazawa, M. Hashimoto, Y. Inouye, and S. Kawata, "Local enhancement of coherent anti-Stokes Raman scattering by isolated gold nanoparticles," J. Raman Spectrosc. **34**, 651–654 (2003).
29. T.-W. Koo, S. Chan, and A. A. Berlin, "Single-molecule detection of biomolecules by surface-enhanced coherent anti-Stokes Raman scattering," Opt. Lett. **30**, 1024–1026 (2005).
30. C. Steuwe, C. F. Kaminski, J. J. Baumberg, and S. Mahajan, "Surface enhanced coherent anti-Stokes Raman scattering on nanostructured gold surfaces," Nano Lett. **11**, 5339–5343 (2011).
31. T.-W. Koo, S. Chan, and A. A. Berlin, "Time-resolved surface-enhanced coherent sensing of nanoscale molecular complexes," Sci. Rep. **2**, 891 (2012).
32. Y. Zhang, Y.-R. Zhen, O. Neumann, J. K. Day, P. Nordlander, and N. J. Halas, "Coherent anti-Stokes Raman scattering with single-molecule sensitivity using a plasmonic Fano resonance," Nat. Commun. **5**, 4424 (2014).
33. S. Yampolsky, D. A. Fishman, S. Dey, E. Hulkko, M. Banik, E. O. Potma, and V. A. Apkarian, "Seeing a single molecule vibrate through time-resolved coherent anti-Stokes Raman scattering," Nat. Photonics **8**, 650–656 (2014).
34. K. T. Crampton, A. Zeytunyan, A. S. Fast, F. T. Ladani, A. Alfonso-Garcia, M. Banik, S. Yampolsky, D. A. Fishman, E. O. Potma, and V. A. Apkarian, "Ultrafast coherent Raman scattering at plasmonic nanojunctions," J. Phys. Chem. C, doi: 10.1021/acs.jpcc.6b02760 (to be published).
35. H. Chew, D. S. Wang, and M. Kerker, "Surface enhancement of coherent anti-Stokes Raman scattering by colloidal spheres," J. Opt. Soc. Am. B **1**, 56–66 (1984).
36. M. Danckwerts and L. Novotny, "Optical frequency mixing at coupled gold nanoparticles," Phys. Rev. Lett. **98**, 026104 (2007).
37. J. Renger, R. Quidant, N. van Hulst, and L. Novotny, "Surface-enhanced nonlinear four-wave-mixing," Phys. Rev. Lett. **104**, 046803 (2010).
38. Y. Wang, C.-Y. Lin, A. Nikolaenko, V. Raghunathan, and E. O. Potma, "Four-wave mixing microscopy of nanostructures," Adv. Opt. Photon. **3**, 1–52 (2011).

39. C. W. Freudiger, W. Min, B. G. Saar, S. Lu, G. R. Holtom, C. He, J. C. Tsai, J. X. Kang, and X. S. Xie, "Label-free biomedical imaging with high sensitivity by stimulated Raman scattering microscopy," Science **322**, 1857–1861 (2008).
40. P. Nandakumar, A. Kovalev, and A. Volkmer, "Vibrational imaging based on stimulated Raman scattering microscopy," New J. Phys. **11**, 033026 (2009).
41. R. R. Frontiera, A. I. Henry, N. L. Gruenke, and R. P. V. Duyne, "Surface-enhanced femtosecond stimulated Raman spectroscopy," J. Phys. Chem. Lett. **2**, 1199–1203 (2011).
42. N. L. Gruenke, M. F. Cardinal, M. O. McAnally, R. R. Frontiera, G. C. Schatz, and R. P. V. Duyne, "Ultrafast and nonlinear surface-enhanced Raman spectroscopy," Chem. Soc. Rev. **45**, 2263–2290 (2016).